JACS
JOURNAL OF THE AMERICAN CHEMICAL SOCIETY
Article
Cite This: J. Am. Chem. Soc. 2018, 140, 1783−1792
pubs.acs.org/JACS

Active Site Revealed for Water Oxidation on Electrochemically Induced δ-MnO_2: Role of Spinel-to-Layer Phase Transition

Ye-Fei Li* and Zhi-Pan Liu*

Collaborative Innovation Center of Chemistry for Energy Material, Key Laboratory of Computational Physical Science (Ministry of Education), Shanghai Key Laboratory of Molecular Catalysis and Innovative Materials, Department of Chemistry, Fudan University, Shanghai 200433, China

Supporting Information

ABSTRACT: Seeking for active MnO_x material as artificial water splitting catalyst has been a long history since the discovery of PSII system in nature. To date, the highest activity MnO_x catalyst reported for oxygen evolution reaction (OER) does however not belong to common MnO_2 polymorphs (α-, β-, δ-MnO_2), but rather to nascent δ-MnO_2 layer produced in situ from spinel under electrochemical conditions with unknown active site structure. Here with the stochastic surface walking (SSW) pathway sampling method, we for the first time resolve the atomic-level mechanism of spinel-to-layer Mn_3O_4 solid phase transition in aqueous electrolyte. We show that a transient $H_{0.5}MnO_2$ phase is the precursor of transition that forms at high voltage (>1 V), and it undergoes the solid-to-solid phase transition to produce a δ-MnO_2 layer, which is accompanied by Mn dissolution, dislocation, layer-breaking, and insertion of water/cations between layers. This leads to the generation of a variety of possible defective structures. We demonstrate using first-principles calculations that a special edge site with neighboring Mn vacancy provides the best OER activity with an overpotential of 0.59 V, 0.19 V lower than that of pristine MnO_2. The high activity of such Mn sites are attributed to its special local structure: pseudocubane with one corner missing. The presence of the Mn vacancy near the active site enhances the adsorption of OH intermediate in OER. This defective cubane structure shares the common geometrical and electronic features found in the PSII system.

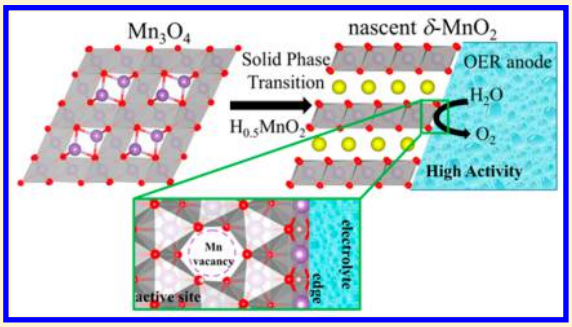

1. INTRODUCTION

In nature, MnO_x-cluster-based PSII system performs oxygen evolution reaction (OER: $H_2O \rightarrow O_2 + 4H^+ + 4e^-$) under sunlight, exhibiting a remarkable activity with an overpotential (η) of 160 mV at pH 6.5.[1−5] MnO_x structures thus hold a great promise as highly active water splitting catalysts. Paradoxically, while synthetic MnO_2 materials, e.g., common polymorphs α- (tetragonal), β- (tetragonal), and δ-MnO_2 (triclinic), do have OER catalytic activity, their activities are generally poor with a high overpotential (>0.6 V at pH < 7).[6−12] The electrochemically induced layer δ-MnO_2 (EI-δ-MnO_2) materials, as found recently, appear to be exceptional: The overpotential is ∼0.54 V at pH 0.3, and thus approaches the performance of precious metal oxides (Ir/RuO_x) under acidic condition.[5,13−15] However, these EI-δ-MnO_2, being poorly crystallized, are produced dynamically from spinel Mn_3O_4 (see Figure 1) under electrochemical OER condition, which has led to a great uncertainty on the structure for the catalytic center at the atomic level. It remains extremely challenging to track down the in situ material evolution, i.e., Mn_3O_4 to δ-MnO_2 transition, and to characterize the active site.

Various experimental techniques have been attempted to probe the nature of nascent EI-δ-MnO_2 in OER. At a nanometer scale, their structures, although poorly crystallized, do appear to share common features with low-activity commercial δ-MnO_2, as confirmed by X-ray diffraction (XRD), X-ray absorption spectroscopy (XAS), X-ray photoelectron spectroscopy (XPS), transmission electron microscopy (TEM), and scanning electron microscopy (SEM) techniques.[12−17] Notably, X-ray absorption near edge structure (XANES) data for EI-δ-MnO_2[14] overlaps with that of triclinic δ-MnO_2 with major peaks at 6560 eV, indicating no significant structural difference between EI-δ-MnO_2 and triclinic δ-MnO_2. It implies that the active sites might be in low concentration and difficult to detect from experiment. However, considering that these active sites are created dynamically in the Mn_3O_4 spinel-to-layer transformation, a better understanding on the solid phase transition may alternatively provide useful hints on the structures of nascent δ-MnO_2. Kim et al. using high-resolution TEM shows that the solid transition turns the spinel Mn_3O_4 (101) plane into the (0001) basal plane of δ-MnO_2 with the layered MnO_2 peeled off from the spinel matrix (Figure 1c,d).[17] This supports a crystal-to-crystal transition mechanism with a $(101)_{sp}//(0001)_{\delta}$ orientation relation. Due to the lack of the atomic information on the pathway, it is still unclear on the likely intermediates of the transition, which might be associated with the OER active site. In fact, similar

Received: October 25, 2017
Published: January 15, 2018

DOI: 10.1021/jacs.7b11393
J. Am. Chem. Soc. 2018, 140, 1783−1792

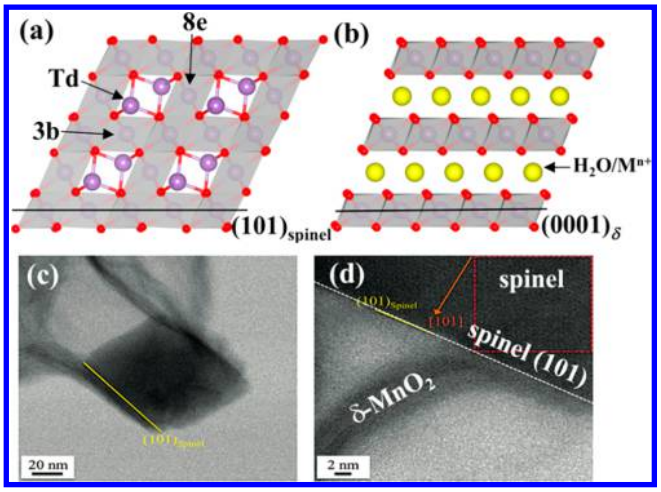

Figure 1. Crystal structures of (a) spinel Mn_3O_4 (#141, $I41/AMD$) and (b) layered δ-MnO_2 (#166, $R\bar{3}m$) in polyhedral representations. (c) The morphology change during spinel-to-layer transition as revealed from Kim's TEM.[17] In panel (c), the layered δ-MnO_2 sheets gradually peel off from spinel surface, and panel (d) shows the enlarged local view where the layered δ-MnO_2 sheet starts to drop from pristine spinel surface. Reprinted with permission from ref 17. Copyright 2015 Wiley.

electrochemically induced activation was observed for other oxides, i.e., CoO_x[18,19] and NiO_x,[20] under the same OER condition, suggesting the general significance for understanding the solid phase transition to identify the active site.

Geometrically, spinel Mn_3O_4 (14_1, $I41/AMD$) and δ-MnO_2 (166, $R\bar{3}m$) phase (Figure 1a,b) are rather different. To obey the observed $(101)_{sp}//(0001)_{\delta}$ orientation relation, the solid phase transition must involve $^1/_4$ octahedron (O_h) Mn ions migration from the 8e Wyckoff position to the 3b position (see Figure 1), not only a long-distance diffusion (~4 Å) but also one requiring breakage of least five Mn−O bonds. In the meantime, since the chemical composition Mn:O is reduced from 3:4 to 1:2, the Mn at the tetrahedron site (T_d) is expected to leave the spinel crystal after the phase transition. The spinel-to-layer transition is therefore structurally complex and cannot be assigned simply as a diffusionless crystal phase transition, e.g., dominated by shearing (Martensitic-type).

Despite their distinct crystal structure and diffusion nature in transition, the spinel-to-layer phase transition, interestingly, can occur in either the forward or reverse direction under different chemical conditions. In the presence of aqueous electrolytes, the spinel-to-layer phase transition can occur rapidly at room temperature, typically within a single cycle of OER.[13−17] The presence of aqueous solution was suggested to promote the dissolution of T_d Mn cations (Figure 1) and the refilling of 8e Mn into the vacant 3b position,[16,17] considering that hydronium (H_3O^+) ions have been detected in the interior of the final layer-like structures.[16] By contrast, with other nonaqueous electrolytes, such as ethylene carbonate in Li-ion batteries, only the reverse layer-to-spinel phase transition[21−24] is observed (and it affects markedly the battery performance).[25] These experiments support the idea that spinel-to-layer transition, unlike common solid-to-solid transitions,[26−29] is open to the environment and couples strongly with the external molecules/ions, which indeed provides a battle ground to form the active site for OER involving H_2O, O_2, and likely OOH intermediates.

Here we utilize our recently developed stochastic surface walking (SSW) method in combination with first-principles density functional theory (DFT) calculations to resolve the OER active site in EI-δ-MnO_2. By sampling the spinel-to-layer solid phase transition pathways exhaustively, we reveal for the first time the lowest energy reaction pathway linking the two phases. Two intermediate phases in the pathway are discovered, which provide direct atomic models to construct the OER active sites. By modeling a number of likely MnO_x reaction centers and computing their OER activity, we characterize the active site of OER as the $(0001)_{\delta}/[11\bar{2}0]$ edge sites with nearby Mn vacancies (edge-NV). We show that the active sites are created dynamically by breaking spinel (101) plane, as caused by the large strain developed in the solid phase transition.

This paper is organized as follows. In section 2, we describe the SSW-based theoretical methods and DFT calculation details. Our main results on the reaction pathway for spinel-to-layer transition and the screening of OER active sites are presented in section 3. Last, we compare the atomic structure of the identified active site with MnO_x cluster in PSII system in section 4.

2. METHODS AND CALCULATION DETAILS

2.1. SSW Reaction Pathway Sampling. In this work, the spinel-to-layer solid phase transition was investigated using the variable-cell SSW reaction pathway sampling (SSW-RS) method.[26−28,30−33] The SSW-RS algorithm was described in our previous work in detail.[30−33] It includes basically two parts: (i) SSW pathway sampling to identify all possible reaction coordinates and (ii) variable-cell double-ended surface walking (VC-DESW) method to locate the transition state (TS) in low energy reaction pathway (also see the Supporting Information for methodology). The SSW-RS was utilized recently in finding the lowest energy pathway of solid phase transition (ZrO_2,[26] TiO_2,[27] MnO_2,[28] and graphite).[29]

For the spinel-to-layer transition, it is technically more difficult to simulate directly the transition using SSW-RS because of the varied chemical composition and the likely participation of external molecules/ions in the reaction. To solve the problem, we took an indirect, three-step approach to determine the lowest energy pathway from spinel to δ-MnO_2, which involves the utilization of $Li_{0.5}MnO_2$ spinel to speed up the pathway sampling. The details of the modeling can be found in the Supporting Information. Starting from $Li_{0.5}MnO_2$, 20 SSW-RS jobs for each phase were run massively parallel. With 2000 SSW sampling steps, 320 pathways were collected, from which 10 low-energy pathways with barriers lower than 0.7 eV/f.u. were identified. Last, we replaced Li with H atoms ($H_{0.5}MnO_2$) and calculated all the reaction pathways using the VC-DESW method.[30−33] All located TSs have been confirmed by extrapolating the TS toward the IS and FS and also the numerical vibrational frequency analysis. The animations of transition pathways are provided in the Supporting Information.

2.2. Calculation Details. DFT calculations were utilized for both SSW pathway sampling and computing energetics of reaction pathways. All DFT calculations were carried out within the periodic plane wave framework as implemented in Vienna ab initio simulation package (VASP).[34] The electron−ion interaction was represented by the projector augmented wave (PAW) and the kinetic energy cutoff of plane wave was set as 500 eV. The exchange-correlation functional utilized was the GGA-PBE[35] with on-site Coulomb repulsion (PBE+U).[36] The effective U−J terms (U_{eff}) as determined by linear response theory was set as 4.0 eV for Mn.[28] The scheme of PBE+U can generate good geometry structures such as lattice parameters and bond lengths. However, it will predict incorrect electronic structures, e.g., band gap and magnetism, and thermodynamics for MnO_2 polymorphs, according to previous study.[28] To overcome this problem, the higher-level methodology such as hybrid functional is desirable to further converge the energetics. In this study, the energetics of all key structures, i.e., initial, transition, and final states, optimized with PBE+U were further recomputed using the hybrid HSE06.[37] For all the Mn-containing systems, the spin-polarization has

DOI: 10.1021/jacs.7b11393
J. Am. Chem. Soc. 2018, 140, 1783−1792

been considered to identify the ground state electronic configuration. While the most stable spin configuration of the phase is system-dependent, the energy difference between the ferromagnetic and the antiferromagnetic solutions are generally small, below 0.04 eV per MnO_2 formula unit (f.u.).

To estimate the energetics of OER, the solvation energy due to the long-range electrostatic interaction was also computed by a periodic continuum solvation model with a smooth dielectric function.[38−40] The k-point mesh utilized was up to (4 × 4 × 4) in the Monkhorst−Pack scheme, which was verified to be accurate enough for these bulk systems. The geometry convergence criterion was set as 0.01 eV/Å for the maximal component of force and 0.01 GPa for stress.

2.3. Computational Models. The SSW-RS simulation and all the reaction pathway calculations utilized a Mn_4O_8 supercell with Li insertion ($Li_2Mn_4O_8$ for SSW-RS) or H insertion ($H_2Mn_4O_8$ for pathways). For the $Li_2Mn_4O_8$ spinel structure where experimental data is available for comparison, all Mn ions occupy the O_h sites, e.g., 8e and 3b positions in Figure 1a, while Li ions locate in the T_d position (also see Figure 1a). The optimized lattice parameters are a = 5.79 Å, b = 6.02 Å, c = 6.02 Å, α = 58°, β = 61°, and γ = 61°, which agree well the experimental lattice parameters (difference < 3%). The spinel $Li_2Mn_4O_8$ is calculated to be weak antiferromagnetic (AFM), which is 0.006 eV/f.u. more stable than the ferromagnetic (FM) counterpart. As for $H_2Mn_4O_8$, all Mn ions occupy the O_h sites, where H ions attach on lattice O. The optimized lattice parameters are a = 6.16 Å, b = 5.81 Å, c = 6.35 Å, α = 57°, β = 59°, and γ = 57°. The ground state of the spinel $H_2Mn_4O_8$ is weak AFM, 0.004 eV/f.u. more stable than the FM configuration.

To investigate OER activities on pristine spinel Mn_3O_4, δ-MnO_2 and the defects of δ-MnO_2, we have created a series of likely active sites on the $(001)_{sp}$ and $(2\bar{1}16)_{\delta}$, and the structures of the surfaces are shown in Figure 2. $(001)_{sp}$, i.e., Mn_3O_4 (001), is the favorable facet

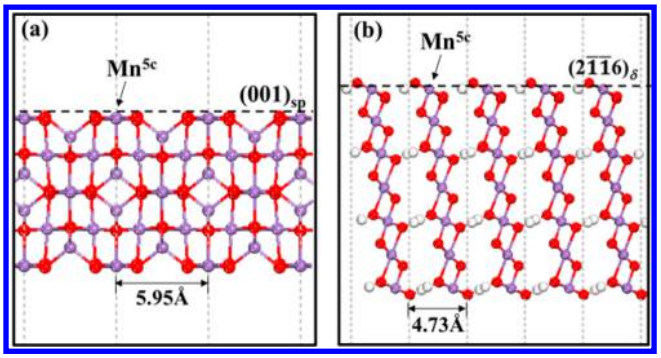

Figure 2. Overview of surface structures for (a) $(001)_{sp}$ and (b) $(2\bar{1}16)_{\delta}$. Red ball: O; white ball: H; violet ball: Mn.

that spinel structure exposes. $(2\bar{1}16)_{\delta}$ is the edge of MnO_2 layers in δ-MnO_2, which contains unsaturated five-coordinated Mn (Mn^{5c}). We chose (2 × 1) supercell for both $(001)_{sp}$ and $(2\bar{1}16)_{\delta}$ surfaces, which contains four exposed five-coordinated Mn (Mn^{5c}) in each unit cell; thus, the coverage of adsorbed species (such as OH) can vary from $^1/_4$ monolayer (ML) to 1 ML. As the high activity of EI-δ-MnO_2 was observed in acidic condition, we have considered the OER under pH 0 in our calculations and all the free energetics are referred to Standard Hydrogen Electrode (SHE) condition (the details of the free energy computation can be found in Supporting Information). From thermodynamics, we determine the phase diagram in the OER condition, which shows that both surfaces are precovered by mixed phase of $^1/_2$ ML H_2O and $^1/_2$ ML OH (2*H_2O, for details see Figure 3) above 1.23 V NHE.

3. RESULTS AND DISCUSSIONS

3.1. OER Activity on Pristine Spinel Mn_3O_4 and δ-MnO_2. Experimentally, the pristine spinel Mn_3O_4 and δ-MnO_2 are known to have poor OER activity. As a first step, we have

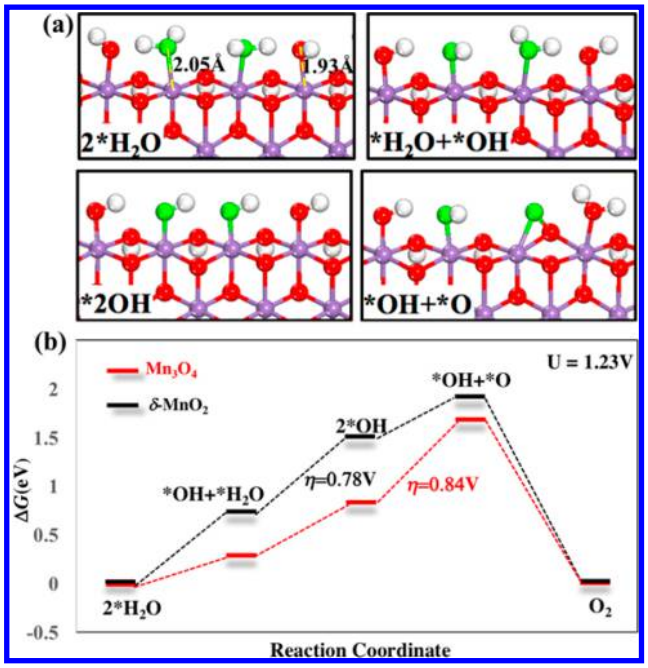

Figure 3. (a) Structures for key intermediates of OER on the edge site of δ-MnO_2 (also see Figure 2b for the edge model). As shown, the surface is covered by terminal OH and newcoming H_2O (O in green ball) adsorb on the top of Mn^{5c}. The geometries of intermediates of OER on spinel Mn_3O_4 is similar as that on δ-MnO_2 and thus is not depicted in this figure. (b) Energetic profiles for OER on Mn_3O_4 and δ-MnO_2. Red ball: O; green ball: O of incoming H_2O; white ball: H; violet ball: Mn.

utilized the thermodynamics approach to analyze the activity for OER on pristine spinel Mn_3O_4 (001) and δ-MnO_2 $(2\bar{1}16)$. The calculated activity as indicated by overpotential can then be a good benchmark for understanding the improved activity of nascent poorly crystallized EI-δ-MnO_2.

Because both surfaces expose terminal OH groups and adsorbed H_2O under OER high potential conditions (see reaction iii and the Supporting Information for phase diagram), we have considered OER on both surfaces following two possible mechanism, either $H_2O \rightarrow OH \rightarrow O \rightarrow O_2$ (reactions i−iv) or $H_2O \rightarrow OH \rightarrow OOH \rightarrow O_2$(reactions i, ii, v, and vi). The surface OH and O and OOH are key intermediates.

$$2^*H_2O \rightarrow {}^*OH + {}^*H_2O + H^+ + e^- \quad \text{(i)}$$

$${}^*OH + {}^*H_2O \rightarrow 2^*OH + H^+ + e^- \quad \text{(ii)}$$

$$2^*OH \rightarrow {}^*OH^* + {}^*O + H^+ + e^- \quad \text{(iii)}$$

$${}^*OH + {}^*O \rightarrow O_2(g) + H^+ + e^- \quad \text{(iv)}$$

or

$${}^*2OH \rightarrow {}^*OOH + H^+ + e^- \quad \text{(v)}$$

$${}^*OOH \rightarrow {}^* + O_2 + H^+ + e^- \quad \text{(vi)}$$

In the formula, the asterisk * denotes the edge Mn^{5c} sites of layered MnO_2. In reactions i and ii, two protons of two water molecules release sequentially into the aqueous solution, resulting in 1 ML OH covered surface (2*OH, Figure 3). Then in reaction iii, a proton of *OH further releases, and the remaining O atom lies down to bond with lattice O to form O−O peroxo species (*OH+*O, Figure 3). In reaction iv, the

DOI: 10.1021/jacs.7b11393
J. Am. Chem. Soc. 2018, 140, 1783−1792

fourth proton releases and O_2 molecule evolves from the surface. Alternatively, the surface adsorbed OH may recombine to form OOH. In reactions i and ii, two protons release from two adsorbed water molecules sequentially to form *2OH. Next, a proton of *OH further releases, and the remaining *O atom bonds with *OH to form *OOH in reaction v. In reaction vi, the proton of *OOH dissolves into aqueous solution, which releases O_2 molecule.

The energetic profiles and intermediate states are shown in Figure 3. For the pristine spinel Mn_3O_4 (001) and δ-MnO_2 ($2\bar{1}16$) the lowest energy pathway follows the $H_2O \rightarrow OH \rightarrow O \rightarrow O_2$ (reactions i–iv) mechanism. On spinel Mn_3O_4 surface, the most endothermic step is reaction iii, which requires an overpotential of 0.84 V at an external potential of U = 1.23 V (equilibrium potential for oxygen evolution reaction at standard condition). While for δ-MnO_2, the most endothermic step is reaction ii, with an overpotential of 0.78 V at U = 1.23 V. The calculated overpotential of δ-MnO_2 (0.78 V) is consistent with experimental overpotential of 0.74 V[6]. Such high overpotentials indicates the observed enhanced OER on EI-δ-MnO_2 cannot be attributed to the intrinsic activity of the reactant and products (spinel Mn_3O_4 and δ-MnO_2)

3.2. Spinel-to-Layer Solid Phase Transition. In order to identify the active site of OER on EI-δ-MnO_2, we have first investigated the solid phase transition from spinel to layer. The metastable intermediates during the phase transition will then be focused and considered as potential active species for OER.

3.2.1. Precursor Spinel Phase Initiating the Phase Transition. Experimentally, the dissolution of T_d site Mn^{2+} for the spinel Mn_3O_4 electrode occurs rapidly even below 0.9 V[17] and therefore the initial state for the spinel-to-layer phase transition is unlikely to be the pristine Mn_3O_4. To balance the net charge of the material, external caions **Y** in aqueous electrolyte (such as H^+) will refill part of the T_d sites, resulting in new $\mathbf{Y}_x$$MnO_2$ phases. The process can be schematically explained in Figure 5a. In this work, we have considered a group of ions, including H^+, Ca^{2+}, Na^+, Mg^{2+}, Li^+, and hydronium (H_3O^+). While large-sized Ca^{2+}, Na^+, and hydronium (H_3O^+) cannot insert into the small tunnel of spinel phase, we have also ruled out the middle-sized ions Mg^{2+} and Li^+ as the initial state for the spinel-to-layer phase transition because of their endothermicity from spinel to layer (see Table 1 in the Supportiong Information). However, the insertion of proton into MnO_2 will result in the exothermicity of the spinel-to-layer phase transition.

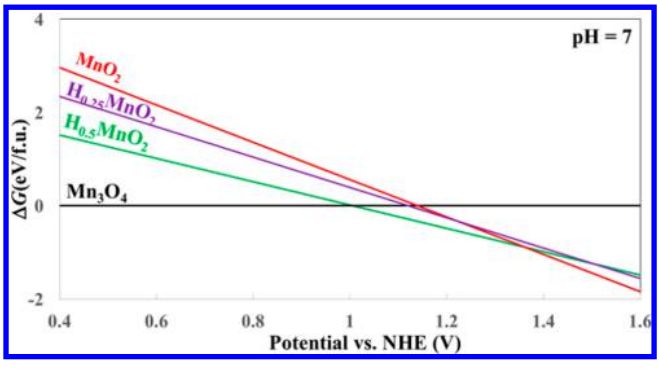

Figure 4. Calculated phase diagram for spinel Mn_3O_4, $H_{0.5}MnO_2$, $H_{0.25}MnO_2$, and MnO_2 at pH 7.

In Figure 4, we show the phase diagram at pH 7 involving three consecutive reactions from spinel Mn_3O_4 to H_xMnO_2 and to MnO_2 following the chemical formula below.

$$2Mn_3O_4 + 4H_2O \rightarrow 6H_{0.5}MnO_2 + 5H^+ + 5e^- \quad (1)$$

$$4H_{0.5}MnO_2 \rightarrow 4H_{0.25}MnO_2 + H^+ + e^- \quad (2)$$

$$4H_{0.25}MnO_2 \rightarrow 4MnO_2 + H^+ + e^- \quad (3)$$

Since the initial Mn_3O_4 phase is taken as the reference, its free energy is set as zero (the horizontal line in phase diagram). The calculation details of the phase diagram can be found in the Supporting Information. Our results show that pristine Mn_3O_4 is stable in low potential less than 1 V, which is consistent with the experimental finding on the poor stability of pristine Mn_3O_4 under neutral electrochemical condition. Above 1 V, $H_{0.5}MnO_2$ becomes the most stable phase, and it gradually loses protons at higher potentials, which eventually reaches to MnO_2 at 1.35 V. In experiment, Kim et al. observed the spinel-to-layer phase transition at the voltage range of 0.9–1.1 V in 1 M Mg_2SO_4 electrolyte but the chemical composition for the initial spinel phase is unknown.[17] From our results, the initial spinel phase is most likely $H_{0.5}MnO_2$ formed in reaction 1, and $H_{0.5}MnO_2$ can undergo further spinel-to-layer transition. In the following, we will utilize the SSW pathway sampling to identify the reaction pathway from spinel $H_{0.5}MnO_2$ to layer $H_{0.5}MnO_2$.

3.2.2. Mechanisms and Kinetics. Starting from the spinel $H_{0.5}MnO_2$ phase, we have determined the lowest energy pathway for the formation of layer MnO_2 based on SSW reaction sampling (reaction i). The energetic profiles and key intermediate structures for reaction pathway are shown in Figure 5 and Table 1. Since the proton transfer is typically less than 0.13 eV/f.u., much lower than the migration barrier of Mn ions, Figure 5 only depicts those events related to Mn displacement (the scenarios involving proton transfer can be found in Figure S2).

The lowest energy pathway of the spinel-to-layer transition contains three major steps (see Figure 5b) with a highest reaction of 0.35 eV/f.u. relating to the insertion of Mn into 3b position. As shown in Figure 5c, the first step, spinel → TS1 → MS1, involves the migration of intercalated Mn (Mn^{ic}, as indicated by arrow in the spinel phase of Figure 5c) caused by shearing movement of MnO_2 layers along $[1\bar{2}10]$ (as evident from the large deformation of spinel lattice, ~15° change in the lattice β angle in Table 1). As a result, Mn^{ic} shifts from **A** to **B** site (see Figure 5c) relative to bottom MnO_2 layer but remains unchanged with respect to the top MnO_2 layer. This step has a barrier of 0.29 eV/f.u. At the transition state (TS), i.e., TS1, Mn^{ic} locates at the lattice O bridge site between **A** and **B** sites, leading to the decrease of coordination number (CN) for the Mn^{ic} from 6 at the IS to 5 at the TS.

MS1 → TS2 → MS2 of Figure 5c shows the reaction snapshots for the second step. This step involves the migration of Mn^{ic} by ~2.5 Å assisted by a shearing movement of MnO_2 layers along $[11\bar{2}0]$ by ~$^1/_2$ lattice. As a result, Mn^{ic} occupies an interlayer position right above a Mn vacancy in **B** site of MnO_2 layer (also see Movie S1). Due to the small structural difference from the MS1 to the MS2, this step is facile with low reaction barrier of 0.05 eV/f.u. and is almost thermoneutral.

MS2 → TS3 → δ-MnO_2 of Figure 5c shows the snapshots for the third step. This step involves the embedding of Mn^{ic} ion toward the Mn vacancy of MnO_2 layer, resulting in a layered structure. In TS3, Mn^{ic} locates in the O plane of MnO_2 layer,

DOI: 10.1021/jacs.7b11393
J. Am. Chem. Soc. 2018, 140, 1783–1792

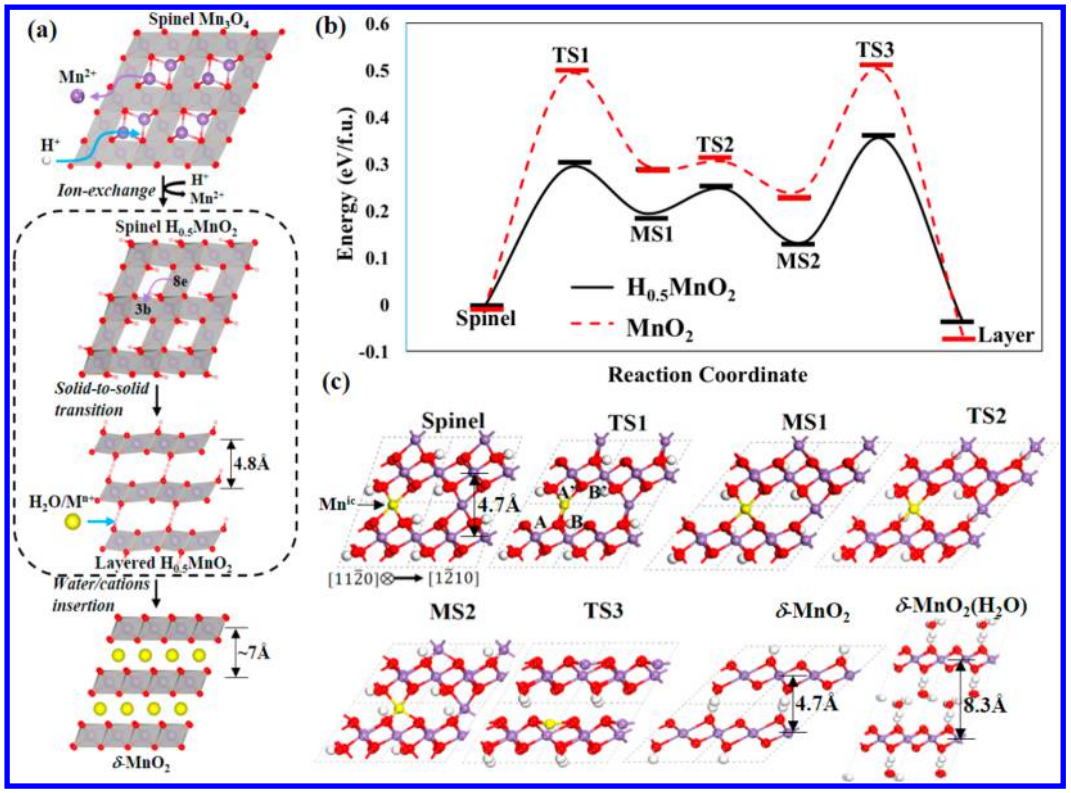

Figure 5. (a) Scheme for the mechanism of spinel-to-layer phase transition (the dotted box indicates the solid-to-solid phase transition step of spinel $H_{0.5}MnO_2$). (b) Energetic profiles for solid-to-solid phase transition of $H_{0.5}MnO_2$ (black solid curve) and MnO_2 (red dashed curve). (c) Side view of key intermediate states of $H_{0.5}MnO_2$ during phase transition viewed from $[11\bar{2}0]$ (using δ-MnO_2 as the reference). In panel (c), the octahedral sites along **A** row are all occupied by Mn ions, while only half of the octahedral sites along **B** raw are occupied, forming an ordered Mn-vacancy structure in the MnO_2 layers. Red ball: O; white ball: H; violet ball: Mn; yellow ball: Mn^{ic}.

Table 1. Geometry, Electronic Structure and Relative Energy for Key Intermediate Phase during Spinel-to-Layer Phase Transition

stru.	CN	spin on Mn^{ic} (μ_B)	**A** deg.	**B** deg.	Mn−O (Å)[a]	ΔE (eV/f.u.)
spinel	6	3.77	57	58	2.26	0
TS1	5	3.90	59	52	3.44	0.29
MS1	6	3.77	51	43	2.33	0.19
TS2	6	3.80	50	42	2.36	0.25
MS2	5	3.78	40	46	2.16	0.13
TS3	4	3.70	39	52	2.67	0.35
δ-MnO_2	6	3.78	49	38	2.36	−0.04

[a]The typical Mn−O bond length for stable intermediate phases, or the bond length for breaking Mn−O bond in TS.

while the CN of Mn^{ic} in TS3 decreases from 6 to 4, where all bonds of Mn^{ic} with the top MnO_2 layer break at this state. Such significant structural change causes a large barrier of 0.35 eV/f.u, and is the rate-determining step in the spinel-to-layer phase transition.

We would like to emphasize that the electron transfer occurs within the MnO_2 layer during the whole process of the phase transition. The oxidation state of Mn^{ic} remain intact as Mn^{3+}, while the Mn^{3+}/Mn^{4+} cations inside the MnO_2 layer exchange their positions during the reaction. At the stage of spinel, Mn^{3+} locates in A site of MnO_2 layer (see Figure 5c for **A** site), whereas Mn^{3+} changes to the **B** site in MS1 and then changes back to **A** site in MS2 and δ-MnO_2. It should be mentioned that from our results, $Mn^{3+}O_6$ octahedra in spinel $H_{0.5}MnO_2$ and δ-MnO_2 have the traditional Jahn−Teller distortions with the axial Mn−O bond being 2.2 Å, slightly longer than the four equatorial Mn−O bonds being 1.9 Å.

After the phase transition, the nascent δ-MnO_2 has a 4.8 Å spacing between layers connected via hydrogen bonds. Our calculations show that the energy change (ΔE) for further inserting external water molecules from aqueous solution into nascent $H_{0.5}MnO_2$ is exothermic by 0.15 eV per water molecule. With the presence of water molecules, the δ-MnO_2 is thus better stabilized and reaches to a large spacing between layers (8.3 Å), forming hydrated δ-$MnO_2(H_2O)$.

Overall, the spinel-to-layer phase transition, despite its great structural complexity, may be simplified as two sequential shearing movements of MnO_2 layers coupled with a long-range Mn^{ic} diffusion. The first shearing occurs along $[1\bar{2}10]$ that induces the Mn^{ic} migration from **A** to **B** site along the direction (Spinel-to-MS1). The second shearing occurs along $[11\bar{2}0]$, which further leads to the Mn^{ic} to occupy an interlayer position right above a Mn vacancy of MnO_2 layer (MS1-to-MS2). Finally, the Mn^{ic} sinks into MnO_2 layer to heal the Mn vacancy (MS2-to-layer). This crystal-to-crystal phase transition follows the orientation relations (OR) of $(0001)_\delta//(101)_{sp}$, $[11\bar{2}0]_\delta//[010]_{sp}$.

As the shearing movement dominates the phase transition, a large strain due to the mismatched interface develops along $[2\bar{1}\bar{1}0]$ (see Figure S3). We note that in the transition the strain along $[2\bar{1}\bar{1}0]$ is up to ~9% which is much larger than typical Martensitic solid phase (~1% in ZrO_2[26]). As a result, one may expect that δ-MnO_2 layers once formed would prefer to peel off from the spinel matrix and may further break apart at $[2\bar{1}\bar{1}0]$ to

DOI: 10.1021/jacs.7b11393
J. Am. Chem. Soc. 2018, 140, 1783−1792

release the strain and forms the MnO_2 $(2\bar{1}\bar{1}6)$ edges. Indeed, TEM images by Kim show that when certain layers (~10 nm) of δ-MnO_2 form on Mn_3O_4 (101) the nascent δ-MnO_2 would peel off from the spinel surface as shown in Figure 1c.[17] In addition, Huynh observed using TEM that the particle size of EI-δ-MnO_2 decreases from 8−10 nm to 2−4 nm after the spinel-to-layer transition.[5]

Our mechanism for the spinel-to-layer solid phase transition is consistent with known experimental observations. First, the interlayer spacing for our layer product in $H_{0.5}MnO_2$ δ-MnO_2 is 4.7 Å, which is similar to the interlayer distance of 4.8 Å for a precursory phase observed in TEM image before the final δ-MnO_2 forms.[17] The final δ-MnO_2 contains inserted H_2O and thus has an even larger interlayer spacing, 7.2 Å from experiment and 8.3 Å from our results. Second, the OR relation $(0001)_\delta//(101)_{sp}$ and $[11\bar{2}0]_\delta//[010]_{sp}$ from our lowest energy pathway is consistent with TEM images that the spinel transits to δ-MnO_2 layer-by-layer on the (101) surface of Mn_3O_4 (see Figure 1c).[17]

It is interesting to examine whether the spinel-to-layer phase transition can occur under the nonaquesous condition. In Figure 5b, we have calculated the reaction pathway of pure MnO_2 transition from spinel to layer with the same reaction pathway as that of $H_{0.5}MnO_2$. We found that the highest barrier for MnO_2 is 0.49 eV/f.u., which is much higher than that in $H_{0.5}MnO_2$ (0.35 eV/f.u.). By analyzing the oxidation state during phase transition, we found Mn^{ic} is Mn^{4+} in MnO_2, which is higher than that in $H_{0.5}MnO_2$. As expected from ionic bonding nature in Mn−O bond, the migration of Mn^{4+} should be more difficult than Mn^{3+} in reaction. We can conclude that the presence of proton leads to the reduction of Mn that promotes the spinel-to-layer phase transition. We emphasize that the water molecules should not participate directly in the phase transition because the solid phase transition occurs in the bulk and the water molecule is too large to fit into the small tunnel of spinel.

Therefore, the promotional effects of the aqueous solution for spinel-to-layer transition include both thermodynamics and kinetics effects. The former helps to stabilize the spinel $H_{0.5}MnO_2$ phase leading to the most stable phase under OER condition and the latter, by inserting protons, reduces Mn^{ic} from Mn^{4+} to Mn^{3+} and lowers the phase transition barrier.

3.3. Structures and OER Activities of Electrochemically Induced Defects. On the basis of the solid phase transition pathway, we are now at the position to conceive the structural defects that might be introduced during the transition. Three new defected structural patterns are proposed as shown in Figure 6.

3.3.1. Electronic Structures. Before we investigated the OER activity on these possible reaction sites, we have analyzed their electronic structures using hybrid DFT calculations (HSE06). Figure 7a shows the density of states (DOS) for these defective sites that is compared with that of the pristine $(0001)_\delta/[11\bar{2}0]$ edge. Since both valence band maxima (VBM) and conductive band minima (CBM) locate in the majority spin for all the cases, we only plot the majority spin component in Figure 7a. The VBM and CBM are mainly contributed from Mn^{3+} (e_g) and Mn^{4+} (e_g) based on the octahedral splitting of Mn cations.

The DOS show the electronic structures are sensitive to the local structures. By aligning the DOS using vacuum level, it is found that the VBM of edge-NV is higher (more positive), while the CBM is lower than those of the pristine edge, respectively. As a result, the band gap decreases from 1.8 to 1.2

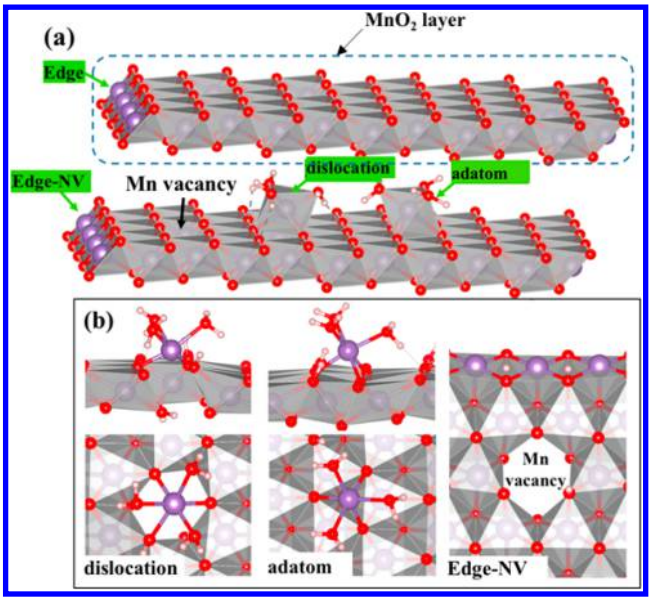

Figure 6. Four possible defected structures in EI-δ-MnO_2. (i) pristine edge (Edge): $(0001)_\delta/[11\bar{2}0]$ edge; (ii) Edge-NV: $(0001)_\delta/[11\bar{2}0]$ edge with nearby Mn vacancy (Pattern 1); (iii) dislocation: Mn^{ic} octahedron above the cationic vacancies of MnO_2 layer (Pattern 2); (iv) adatom: Mn adatom adsorbed on a vacancy-free MnO_2 layer (Pattern 3). Pattern 1 is the $(0001)_\delta/[11\bar{2}0]$ edge with nearby Mn cationic vacancy (edge-NV), which can be generated during MS2 → layer, where Mn^{ic} at the stage of MS2 dissolves into the electrolyte. Pattern 2 is the dislocation of Mn^{ic}, where Mn^{ic} locates above the cationic vacancies of MnO_2 layer, bonding with three water and three lattice O. This pattern can also be generated during MS2 → layer, where Mn^{ic} stays at the stage of the MS2 and does not sinks into MnO_2 layer. Pattern 3 is an Mn adatom adsorbed on a vacancy-free MnO_2 layer, where Mn^{ic} bonds with three water and three lattice O. This pattern can be generated at the final stage of phase transition, where the Mn cations from electrolyte deposits onto the perfect δ-MnO_2.

eV when a vacancy is created near the pristine edge. The presence of one Mn cationic vacancy decreases the total magnetic moment by 7 μ_B, indicating the presence of vacancy leads to the creation of additional four Mn^{4+} in MnO_2 layer. This indicates the formation of a local high concentration of Mn^{4+}. By plotting the VBM and CBM of edge-NV (Figure 7b,c) and the pristine edge, we found the newly created Mn^{4+} ions are around the vacancy, e.g., Mn7 in Figure 7b. It is noticed that the wave functions of VBM and CBM of edge-NV are not localized on particular Mn^{3+} but spread on Mn cations from the edge to the bulk around the vacancy.

As for dislocation and adatom structures, the DOS show that the positions of VBM and CBM overlap, resulting in a band gap of 1.3 eV. In both systems, VBM and CBM are lower (more negative) than those in the pristine edge, as shown in Figure 7a. The total magnetic moment of dislocation did not change comparing to pristine δ-MnO_2, and no new Mn^{3+} are introduced in this structure. As for adatom structure, the total magnetic moment increases by 3 μ_B, indicating the concentration of Mn^{3+} in MnO_2 layer increases, due to the electron injection from Mn adatom into MnO_2 layer. It should be mentioned that the wave functions of VBM and CBM also delocalize (see the Supporting Information).

3.3.2. OER Activities. Since defective sites of Mn dislocation, adatom and edge-NV have distinct electronic structure, one may expect they could be quite different in the OER activity.

DOI: 10.1021/jacs.7b11393
J. Am. Chem. Soc. 2018, 140, 1783−1792

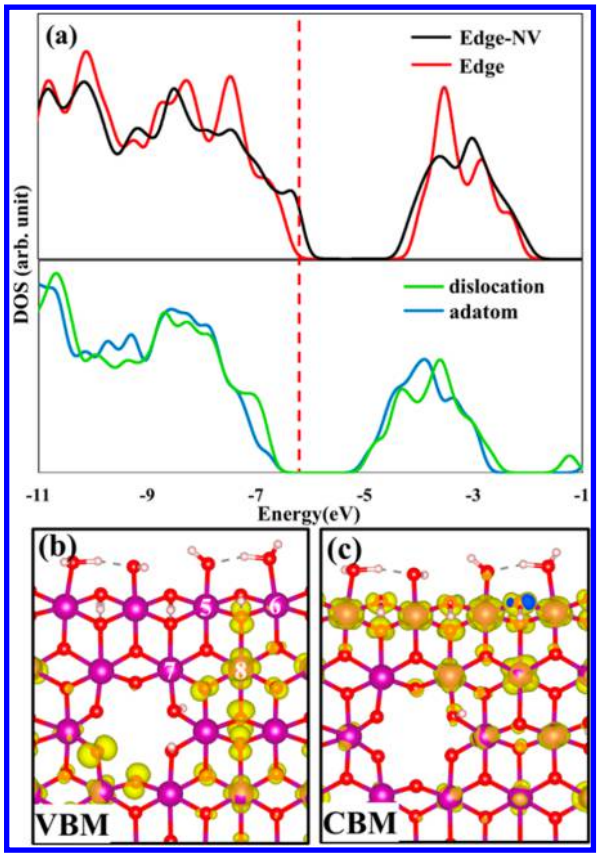

Figure 7. (a) Density of states (DOS) of majority spin for pristine edge (Edge) and three defective sites (Edge-NV, dislocation and adatom). The red dashed line indicates the VBM of pristine edge. All DOS are aligned using vacuum level as reference. (b and c) 3D isosurface contour plot for VBM and CBM of $(0001)_\delta/[11\bar{2}0]$ edge with nearby Mn cationic vacancy (Edge-NV in panel (a)), where the isosurface value is set as 0.0023 (e/Å^3).[2]

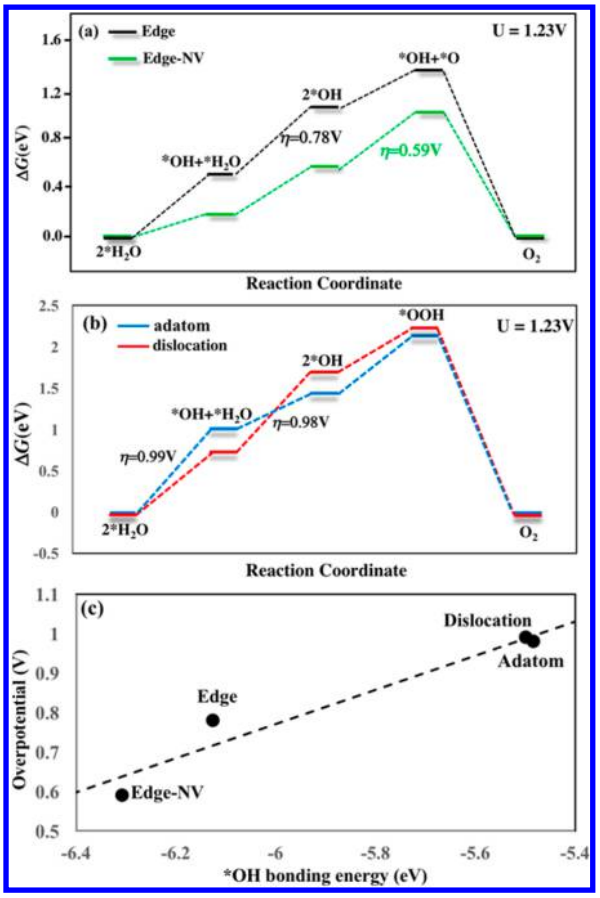

Figure 8. Energetic profiles for OER on (a) pristine edge and edge-NV as well as (b) adatom and dislocation structures. (c) Correlation between calculated overpotentials and *OH bonding energies on four reaction sites.

To determine which defect might be the active site for OER, we then investigate the mechanisms of OER on three defective structures following the two mechanisms in formula (i)-(vi). For edge-NV, the mechanism is the same as to that on pristine edge site (see Figure 3), involving OH and O as the key intermediates. For Mn dislocation and Mn adatom, the mechanisms of OER are different, involving OH and OOH as the key intermediate with the four reactions i–iv.

The energetic profiles for the OER on these defected sites are plotted in Figure 8. We found edge-NV is more active than pristine edge of δ-MnO_2. The calculated overpotential on edge-NV is 0.59 V, which is 0.19 eV lower than pristine edge. By using microkinetics, we deduce that a 0.19 V overpotential reduction would lead to three-order increase in the reaction rate, supporting the high activity of EI-δ-MnO_2. Experimentally, the measured current density of OER on EI-δ-MnO_2 is 1 mA/cm^2 under 0.6 V overpotential, about 2 orders larger than as prepared MnO_x at the same potential.[5]

For the Mn dislocation and adatom structures, the calculated overpotentials are 0.98 and 0.99 V, even higher than edge site of pristine δ-MnO_2, suggesting they are not the active site for OER. Experimentally, δ-MnO_2 with a significant amount of cationic vacancies and dislocated Mn cations have been synthesized in acidic condition.[41,42] Smith et al. show that these structures with high concentration of Mn dislocations are not active with $\eta > 0.7$ V for OER,.[11] This is consistent with our calculations on the poor activity of Mn dislocation.

To understand the origin of high OER activity on edge-NV, we plotted the overpotentials against the *OH (a key intermediate state in OER) bonding energy with Mn ion, as shown in Figure 8c. There is a good correlation between *OH bonding energy and the calculated overpotentials ($R^2 > 0.9$), indicating that the *OH bonding energy is a good descriptor for OER activities on various reaction sites of EI-δ-MnO_2. From Figure 8c, we found edge-NV have the strongest OH bonding energy, while for OER on other three sites, the *OH bonding energies are at least 0.2 eV lower than edge-NV. This result indicates the adsorptions of OH on edge, Mn dislocation and adatom are too weak, which causes large overpotentials on these reaction sites. As for edge-NV, since the OH adsorption is stronger, *OH can be stabilized on this site, and thus the OER activity is higher than that on other reaction sites.

By aligning the energy levels between free OH radical and MnO_x, we found that the free OH HOMO states are well below the VB of MnO_x (see Figure S5), and thus the OH adsorption on the MnO_x can be characterized as a OH anion on a reduced MnO_x with one electron transfer from MnO_x to *OH. In the edge-NV, the presence of a higher VBM and a lower CBM would facilitate the electron transfer from VBM to the OH and enhance the covalent bonding between OH and Mn[5c]. This can be seen clearly from the charge density difference plot in Figure S6, where the covalent characteristics

DOI: 10.1021/jacs.7b11393
J. Am. Chem. Soc. 2018, 140, 1783–1792

between O 2p and Mn 3d states are more obvious in the OH/edge-NV system compared to the OH/pristine edge.

4. DISCUSSION ON THE ACTIVE SITE STRUCTURES IN PSII SYSTEM AND EI-δ-MNO_2

Finally, it is intriguing to compare the structure of edge-NV, the active site for EI-δ-MnO_2, with the oxygen evolution complex (OEC) in PSII system. Figure 9 depicts the atomic structures

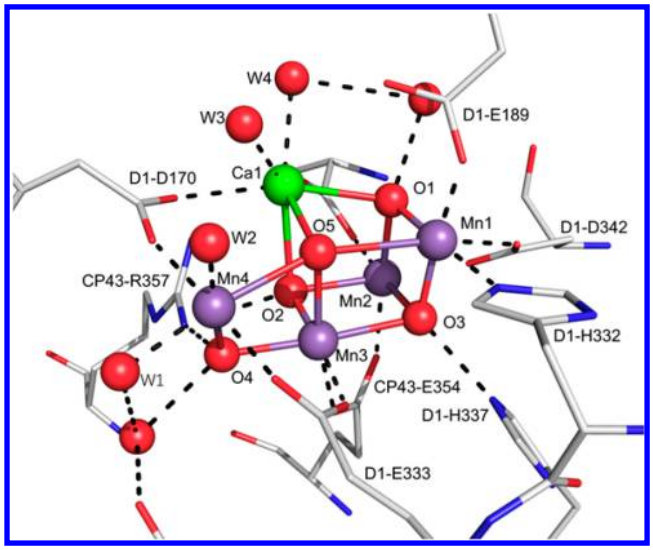

Figure 9. Structure for OEC in PS II system. Reprinted with permission form ref 1. Copyright 2011 Nature Publishing Group and Wikipedia.

for $CaMn_4O_4$ OEC in PS II system resolved recently from experiment,[1] which consists of four Mn (Mn1−Mn4) and one Ca cation. Mn4 locates outside the cubane $CaMn_3O_4$, linking the cubane via two oxo bridges.[1] All four Mn ions are in octahedral coordination with O or N from ligands, e.g., O, H_2O, carboxyl, imidazole, and so on, linking each other via edge-sharing. It is noticed that these octahedra are distorted compared to commercial MnO_2 polymorphs. For instance, ∠Mn3−O5−Mn4, ∠Mn1−O3−Mn3, and ∠Mn2−O3−Mn3 are 78, 107, and 82°, respectively, deviating from the ∠Mn−O−Mn angle 97° in δ-MnO_2 (c.f. 131° in β-MnO_2 with corner-sharing). In parallel with the structural complexity, the oxidation state for Mn ions in OEC are not uniform, where Mn1 and Mn2 are Mn^{4+}, while Mn3 and Mn4 are Mn^{3+} at the S^0 state. Attaching to the $CaMn_4O_4$ cluster, there are four water molecules, two (W1 and W2 in Figure 9) bonding with Mn4 and the other (W3 and W4 in Figure 9) bonding with Ca cation. They are presumably the reactant or proton acceptors for OER.

For the edge-NV in EI-δ-MnO_2, the OER involve two Mn cations (Mn5 and Mn6) during reaction that further link with Mn7, Mn8 as their first neighbor, as shown in Figure 7b. All Mn cations are in edge-sharing MnO_6 octahedra, which are distorted appreciably from the pristine δ-MnO_2 as evident from the angles of ∠Mn5−O−Mn7 (89°) and ∠Mn5−O−Mn8 (106°). The structure of edge-NV is thus close to OEC. Our electronic structure calculations show that the oxidation state of Mn ions in edge site (Mn5, Mn6) are Mn^{4+}, while the neighboring Mn7 and Mn8 are Mn^{3+}. On the edge site, one H_2O or OH bonds with each edge Mn ion.

By comparing the edge-NV and the OEC, we can identify three common features: (i) All Mn ions in both structures are in distorted octahedra with edge-sharing connection. (ii) The edge-NV not only has a corner-missing cubane, i.e., Mn5, Mn6, and Mn8, which not only is comparable with the Mn_3O_4 cubane (Mn1−Mn3) in OEC but also has a Mn vacancy close to the cubane (nearby Mn7). (iii) The oxidation state of Mn ions in both structures is mixed with both Mn^{3+} and Mn^{4+}. Nevertheless, apart from its periodic structure, the edge-NV still differs from the OEC in two aspects. First, no Ca cation is present in edge-NV. Second, the Mn4 cation in PS II system locates outside the cubane, which is structurally closer to the adatom model in Figure 6, but is not present in the edge-NV. For edge-NV, instead, a nearby Mn vacancy is critical for the OER activity.

From the comparison, we conclude that the corner-missing cubane structure unit (with mixed Mn^{3+}/Mn^{4+}) is essence for OER activity and its electronic structure needs to be tuned further to achieve high activity. As shown in Figure 8c, the vacancy neighboring the corner-missing cubane (Mn5, 6, 8) has promoted the adsorption of OH intermediate, which significantly reduces the overpotential in OER. Fundamentally, this is because the upshift of VBM and downshift of CBM caused by the breaking the MnO_6 symmetry in the vacancy site. Interestingly, the $CaMn_4O_4$ OEC in PS II system with an overpotential of 0.16 V[1−5] for OER is still more active than the edge-NV, which suggests that there is still ample room for the improvement of MnO_x catalyst. This may be achieved by doping alkaline metals (Ca^{2+}) and further introducing Mn or other cation adatoms, as practiced recently in experiment.[43−46]

5. CONCLUSIONS

This work represents a comprehensive survey on MnO_x structures as water oxidation catalyst. By first confirming that common MnO_2 phases have a poor OER activity, we determine the lowest energy reaction pathway on the potential energy surface of spinel-to-layer phase transition, which helps to identify the transient MnO_x structures occurring in the solid phase transition. This finally leads to the finding of the active site in the nascent EI-δ-MnO_2 that contributes to its high OER activity. As the current bottom-up approach for investigating catalytic reaction does not require a detailed structure input from experiment, it holds a great promise to reveal the active site and mechanism of complex catalytic system from first principles. Our major conclusions are outlined as follows. (i) A transient $H_{0.5}MnO_2$ phase is first formed before the spinel-to-layer transition. This intermediate phase further undergoes a solid-to-solid phase transition to generate a layered $H_{0.5}MnO_2$, and then water molecules are inserted into the interlayer space, separating and stabilizing the MnO_2 single layers. (ii) The presence of proton is essential for the low barrier spinel-to-layer transition. The rate-determining step of the solid transition is related to the Mn ions embedding into the Mn vacancy of MnO_2 layer, and the whole transition has an overall barrier of 0.35 eV/f.u. In nonaqueous (aprotic) electrolyte, the phase transition becomes kinetically much more difficult, 0.49 eV for the overall barrier. (iii) The spinel-to-layer phase transition proceeds via two sequential shearing movements of MnO_2 layers along with $[1\bar{2}10]$ and $[11\bar{2}0]$, coupled with the long-range Mn^{ic} diffusion. This atomic movement pattern builds a large strain up to 9% between spinel and δ-MnO_2, which may cause the nascent δ-MnO_2 layers to peel off from spinel matrix and further break apart to form new $(0001)_\delta/[11\bar{2}0]$ edges. (iv)

DOI: 10.1021/jacs.7b11393
J. Am. Chem. Soc. 2018, 140, 1783−1792

According to the solid phase transition mechanism, three different local structures, i.e., edge-NV, dislocation, and adatom, are proposed and examined for their OER activity. Only the edge-NV site is active for OER, where the ovepotential decreases by 0.19 V comparing to the pristine edge site. The edge-NV structure has mixed Mn^{3+} and Mn^{4+} cations, and with a Mn vacancy, it introduces a local high concentration of Mn^{4+} near the reaction site. The high activity of edge-NV rationalizes 2 orders of magnitude enhancement of current density observed in experiment on the nascent EI-δ-MnO_2. The enhanced OER activity of the edge-NV site is attributed to the corner-missing cubane local structure unit that promotes the OH intermediate adsorption.

■ ASSOCIATED CONTENT

Supporting Information

The Supporting Information is available free of charge on the ACS Publications website at DOI: 10.1021/jacs.7b11393.

Animation for spinel-to-layer phase transition pattern (AVI)

Details for SSW reaction pathway sampling; calculation details for phase diagram; calculation details for theoratical overpotential; phase diagram for δ-MnO_2 and pristine spinel Mn_3O_4 in aqueous electrolyte; complete energetic profiles (involving proton transfer steps) for solid-to-solid phase transition of $H_{0.5}MnO_2$ and MnO_2; interfacial strain between layer and spinel phases; 3D isosurface contour plot for adatom and dislocation structures; charge density difference for OH adsorption on δ-MnO_2; alignment of energy levels between OH and δ-MnO_2 (PDF)

■ AUTHOR INFORMATION

Corresponding Authors

*E-mail: yefeil@fudan.edu.cn.

*E-mail: zpliu@fudan.edu.cn.

ORCID

Ye-Fei Li: 0000-0003-4433-7433

Zhi-Pan Liu: 0000-0002-2906-5217

Notes

The authors declare no competing financial interest.

■ ACKNOWLEDGMENTS

This work is supported by National Science Foundation of China (21533001, 91545107, 21773032, and 91745201), Science and Technology Commission of Shanghai Municipality (08DZ2270500), Program for Professor of Special Appointment (Eastern Scholar) at Shanghai Institute of Higher Learning, Shanghai Pujiang Program (15PJ1400500), and Shanghai "Chen Guang" project (14CG02).

■ REFERENCES

(1) Umena, Y.; Kawakami, K.; Shen, J.-R.; Kamiya, N. *Nature* **2011**, *473*, 55−60.

(2) Vass, I.; Styring, S. *Biochemistry* **1991**, *30*, 830−839.

(3) Geijer, P.; Morvaridi, F.; Styring, S. *Biochemistry* **2001**, *40*, 10881−10891.

(4) Metz, J. G.; Nixon, P. J.; Rogner, M.; Brudvig, G. W.; Diner, B. A. *Biochemistry* **1989**, *28*, 6960−6969.

(5) Huynh, M.; Shi, C.; Billinge, S. J. L.; Nocera, D. G. *J. Am. Chem. Soc.* **2015**, *137*, 14887−14904.

(6) Meng, Y.; Song, W.; Huang, H.; Ren, Z.; Chen, S.-Y.; Suib, S. L. *J. Am. Chem. Soc.* **2014**, *136*, 11452−11464.

(7) Najafpour, M. M.; Renger, G.; Hołyńska, M.; Moghaddam, A. N.; Aro, E.-M.; Carpentier, R.; Nishihara, H.; Eaton-Rye, J. J.; Shen, J.-R.; Allakhverdiev, S. I. *Chem. Rev.* **2016**, *116*, 2886−2936.

(8) Robinson, D. M.; Go, Y. B.; Mui, M.; Gardner, G.; Zhang, Z.; Mastrogiovanni, D.; Garfunkel, E.; Li, J.; Greenblatt, M.; Dismukes, G. C. *J. Am. Chem. Soc.* **2013**, *135*, 3494−3501.

(9) Takashima, T.; Hashimoto, K.; Nakamura, R. *J. Am. Chem. Soc.* **2012**, *134*, 1519−1527.

(10) Takashima, T.; Hashimoto, K.; Nakamura, R. *J. Am. Chem. Soc.* **2012**, *134*, 18153−18156.

(11) Smith, P. F.; Deibert, B. J.; Kaushik, S.; Gardner, G.; Hwang, S.; Wang, H.; Al-Sharab, J. F.; Garfunkel, E.; Fabris, L.; Li, J.; Dismukes, G. C. *ACS Catal.* **2016**, *6*, 2089−2099.

(12) Iyer, A.; Del-Pilar, J.; King'ondu, C. K.; Kissel, E.; Garces, H. F.; Huang, H.; El-Sawy, A. M.; Dutta, P. K.; Suib, S. L. *J. Phys. Chem. C* **2012**, *116*, 6474−6483.

(13) Gorlin, Y.; Chung, C.-J.; Benck, J. D.; Nordlund, D.; Seitz, L.; Weng, T.-C.; Sokaras, D.; Clemens, B. M.; Jaramillo, T. F. *J. Am. Chem. Soc.* **2014**, *136*, 4920−4926.

(14) Gorlin, Y.; Lassalle-Kaiser, B.; Benck, J. D.; Gul, S.; Webb, S. M.; Yachandra, V. K.; Yano, J.; Jaramillo, T. F. *J. Am. Chem. Soc.* **2013**, *135*, 8525−8534.

(15) Gorlin, Y.; Chung, C.-J.; Nordlund, D.; Clemens, B. M.; Jaramillo, T. F. *ACS Catal.* **2012**, *2*, 2687−2694.

(16) Kim, S.; Lee, S.; Nam, K. W.; Shin, J.; Lim, S. Y.; Cho, W.; Suzuki, K.; Oshima, Y.; Hirayama, M.; Kanno, R.; Choi, J. W. *Chem. Mater.* **2016**, *28*, 5488−5494.

(17) Kim, S.; Nam, K. W.; Lee, S.; Cho, W.; Kim, J.-S.; Kim, B. G.; Oshima, Y.; Kim, J.-S.; Doo, S.-G.; Chang, H.; Aurbach, D.; Choi, J. W. *Angew. Chem., Int. Ed.* **2015**, *54*, 15094−15099.

(18) Wang, H.-Y.; Hung, S.-F.; Chen, H.-Y.; Chan, T.-S.; Chen, H. M.; Liu, B. *J. Am. Chem. Soc.* **2016**, *138*, 36−39.

(19) Yeo, B. S.; Bell, A. T. *J. Am. Chem. Soc.* **2011**, *133*, 5587−5593.

(20) Trotochaud, L.; Ranney, J. K.; Williams, K. N.; Boettcher, S. W. *J. Am. Chem. Soc.* **2012**, *134*, 17253−17261.

(21) Zhang, H.; Karki, K.; Huang, Y.; Whittingham, M. S.; Stach, E. A.; Zhou, G. *J. Phys. Chem. C* **2017**, *121*, 1421−1430.

(22) Armstrong, A. R.; Dupre, N.; Paterson, A. J.; Grey, C. P.; Bruce, P. G. *Chem. Mater.* **2004**, *16*, 3106−3118.

(23) Vitins, G.; West, K. *J. Electrochem. Soc.* **1997**, *144*, 2587−2592.

(24) Kim, S. H.; Im, W. M.; Hong, J. K.; Oh, S. M. *J. Electrochem. Soc.* **2000**, *147*, 413−419.

(25) Armstrong, A. R.; Bruce, P. G. *Nature* **1996**, *381*, 499−500.

(26) Guan, S.-H.; Zhang, X.-J.; Liu, Z.-P. *J. Am. Chem. Soc.* **2015**, *137*, 8010−8013.

(27) Zhu, S.-C.; Xie, S.-H.; Liu, Z.-P. *J. Am. Chem. Soc.* **2015**, *137*, 11532−11539.

(28) Li, Y.-F.; Zhu, S.-C.; Liu, Z.-P. *J. Am. Chem. Soc.* **2016**, *138*, 5371−5379.

(29) Xie, Y.-P.; Zhang, X.-J.; Liu, Z.-P. *J. Am. Chem. Soc.* **2017**, *139*, 2545−2548.

(30) Zhang, X.-J.; Liu, Z.-P. *J. Chem. Theory Comput.* **2015**, *11*, 4885−4894.

(31) Zhang, X.-J.; Shang, C.; Liu, Z.-P. *J. Chem. Theory Comput.* **2013**, *9*, 5745−5753.

(32) Shang, C.; Zhang, X. J.; Liu, Z. P. *Phys. Chem. Chem. Phys.* **2014**, *16*, 17845−56.

(33) Shang, C.; Liu, Z. P. *J. Chem. Theory Comput.* **2013**, *9*, 1838−1845.

(34) Kresse, G.; Furthmüller, J. *Phys. Rev. B: Condens. Matter Mater. Phys.* **1996**, *54*, 11169−11186.

(35) Perdew, J. P.; Burke, K.; Ernzerhof, M. *Phys. Rev. Lett.* **1996**, *77*, 3865−3868.

(36) Anisimov, V. I.; Zaanen, J.; Andersen, O. K. *Phys. Rev. B: Condens. Matter Mater. Phys.* **1991**, *44*, 943−954.

(37) Heyd, J.; Scuseria, G. E.; Ernzerhof, M. *J. Chem. Phys.* **2003**, *118*, 8207−8215.

DOI: 10.1021/jacs.7b11393
J. Am. Chem. Soc. 2018, 140, 1783−1792

(38) Fattebert, J. L.; Gygi, F. *Phys. Rev. B: Condens. Matter Mater. Phys.* **2006**, *73*, 115124.
(39) Li, Y.-F.; Liu, Z.-P.; Liu, L.; Gao, W. *J. Am. Chem. Soc.* **2010**, *132*, 13008−13015.
(40) Fang, Y.-H.; Liu, Z.-P. *J. Am. Chem. Soc.* **2010**, *132*, 18214−18222.
(41) Grangeon, S.; Lanson, B.; Miyata, N.; Tani, Y.; Manceau, A. *Am. Mineral.* **2010**, *95*, 1608.
(42) Grangeon, S.; Manceau, A.; Guilhermet, J.; Gaillot, A.-C.; Lanson, M.; Lanson, B. *Geochim. Cosmochim. Acta* **2012**, *85*, 302−313.
(43) Kang, Q.; Vernisse, L.; Remsing, R. C.; Thenuwara, A. C.; Shumlas, S. L.; McKendry, I. G.; Klein, M. L.; Borguet, E.; Zdilla, M. J.; Strongin, D. R. *J. Am. Chem. Soc.* **2017**, *139*, 1863−1870.
(44) Thenuwara, A. C.; Attanayake, N. H.; Yu, J.; Perdew, J. P.; Elzinga, E. J.; Yan, Q.; Strongin, D. R. *J. Phys. Chem. B* **2017**, DOI: 10.1021/acs.jpcb.7b06935.
(45) Thenuwara, A. C.; Shumlas, S. L.; Attanayake, N. H.; Aulin, Y. V.; McKendry, I. G.; Qiao, Q.; Zhu, Y.; Borguet, E.; Zdilla, M. J.; Strongin, D. R. *ACS Catal.* **2016**, *6*, 7739−7743.
(46) Thenuwara, A. C.; Cerkez, E. B.; Shumlas, S. L.; Attanayake, N. H.; McKendry, I. G.; Frazer, L.; Borguet, E.; Kang, Q.; Remsing, R. C.; Klein, M. L.; Zdilla, M. J.; Strongin, D. R. *Angew. Chem., Int. Ed.* **2016**, *55*, 10381−10385.

DOI: 10.1021/jacs.7b11393
J. Am. Chem. Soc. 2018, 140, 1783−1792